MOBILE LASER SCANNING WITH LOW-COST NAVIGATION SENSORS: COMPENSATING FOR LOW-GRADE IMU WITH DUAL-GNSS AND TIGHTLY-COUPLED LIDAR

Florian Pöppl[1]*, Harald Teufelsbauer[2], Andreas Ullrich[2], Norbert Pfeifer[1]

[1]Technische Universität Wien, Vienna, Austria - (florian.poeppl, norbert.pfeifer)@geo.tuwien.ac.at
[2]RIEGL Laser Measurement Systems GmbH, Horn, Austria - (hteufelsbauer, aullrich)@riegl.com

KEY WORDS: Georeferencing, Sensor Fusion, Sensor Orientation, Kinematic Mapping

ABSTRACT:

Kinematic laser scanning enables efficient and accurate acquisition of 3D data, specifically point clouds. Transforming the laser ranging measurements from the scanner coordinate system to a georeferenced coordinate system requires integration with auxiliary navigation systems, in this case using GNSS (global navigation satellite system) and an IMU (inertial measurement unit). GNSS and IMU data are commonly fused via Kalman filter, and the resulting trajectory is used for georeferencing. Errors in the trajectory propagate through the georeferencing and cause discrepancies in the point cloud. To mitigate this, we present a holistic integration method incorporating GNSS, IMU and LiDAR measurements in a single adjustment, which can be seamlessly adapted to a setup with two GNSS receivers and antennas. This tight coupling of LiDAR and IMU together with the dual-GNSS setup allows the use of an ultra low-cost IMU while still achieving high-quality point clouds. We demonstrate this methodology on two datsets, where we discuss in particular the boresight calibration of such a system, and the impact of the LiDAR measurements and the dual-GNSS set-up on the trajectory and the point cloud.

1. INTRODUCTION

Kinematic laser scanning is a widely used surveying technique for efficient and accurate acquisition of 3D data, specifically point clouds. Laser scanning is based on light detection and ranging (LiDAR) together with a scanning mechanism. Therefore, the measurements are primarily distances together with angles, which are transformed into Cartesian coordinates respective the laser scanner's own coordinate system. Transforming the measurements from the scanner coordinate system to a georeferenced coordinate system requires knowledge of the scanner's position and orientation. This is achieved by integrating auxiliary navigation systems, in this case global navigation satellite system (GNSS) receivers/antennas and an inertial measurement unit (IMU). These two technologies synergize well, as GNSS provides absolute positioning and the IMU provides relative position and orientation through integration of the inertial measurements. The inertial sensors suffer from time-varying measurement errors, which may be calibrated in-run by fusing the IMU with the GNSS measurements in a Kalman filter. However, the resulting trajectory (position and orientation over time) still contains errors, which manifest as discrepancies in overlapping point clouds. These discrepancies can be minimized in a strip adjustment (Glira et al., 2015). A standard processing pipeline in mobile mapping is thus (1) computing a trajectory from GNSS/IMU data, (2) georeferencing of the laser data to a global coordinate system and (3) strip adjustment.

Recently, holistic approaches for GNSS, IMU and LiDAR integration combining these 3 steps have become popular (cf. Pöppl et al. 2023a). Such an integrated approach to sensor fusion is common in robotics (e.g., Chang et al. 2019), but has also been applied to bundle adjustment (Cucci et al., 2017) and airborne laser scanning (Brun et al., 2022). In mobile laser scanning, it is common to use two GNSS receivers/antennas (Wang et al., 2019). The use of two GNSS antennas mounted in a suitable geometric configuration allows estimation of the vehicle heading from the GNSS measurements. In a GNSS/IMU integration, this helps to limit the IMU drift due to increased redundancy, which is especially critical when using low-cost inertial sensors and for data acquisitions with low vehicle dynamics.

In this work, a holistic approach to GNSS/IMU/LiDAR integration is presented, which is seamlessly adapted to a setup with two GNSS antennas. Raw measurements from the IMU, preprocessed position measurements from the GNSS, and LiDAR-derived constraints are incorporated in a single model. This is a tight coupling of IMU and LiDAR and a loose coupling of the GNSS. By tightly coupling IMU and LiDAR, the comparatively high accuracy of the laser scanner can be exploited to correct IMU errors at the sensor level.

2. TRAJECTORY ESTIMATION METHODOLOGY

This sensor fusion approach is based on non-linear least-squares (NLS) estimation, which jointly estimates all parameters: the platform position and orientation, IMU biases and scale factors, GNSS antenna lever-arms and LiDAR mounting parameters, as well as object parameters which model the physical environment. The trajectory is modelled using Euclidean B-Splines for position and quaternion B-Splines for orientation (Kim et al., 1995). This continuous-time parametrization allows to evaluate the trajectory and its derivatives at all measurement times. Thus, model predictions for a given set of parameters can be derived for all measurements: GNSS, IMU, LiDAR. The differences between model predictions and actual measurements are minimized to obtain a set of best-fitting parameters. In contrast to a Kalman filter, where inertial measurements are interpreted as an input to the motion model (Farrell et al., 2022), this formulation does not include (or rather: need) a motion model. This

---

* Corresponding author

approach was recently applied to airborne laser scanning (Pöppl et al., 2023b) and for kinematic usage of a terrestrial laser scanner[1], and thus the following description is based on this prior work.

For a set of n noisy vector-valued measurements $\widetilde{\boldsymbol{y}}_i$ of true values $\boldsymbol{y}_i$, the true values are modelled as a function of unknown parameters $\boldsymbol{x}$, so that

$$\boldsymbol{y}_i := f_i(\boldsymbol{x}), \qquad (2.1)$$

and the measurements $\widetilde{\boldsymbol{y}}_i$ are given as the true values plus noise

$$\begin{aligned} \widetilde{\boldsymbol{y}}_i &:= \boldsymbol{y}_i + \boldsymbol{\epsilon}_i \\ &= f_i(\boldsymbol{x}) + \boldsymbol{\epsilon}_i. \end{aligned} \qquad (2.2)$$

The error term $\boldsymbol{\epsilon}_i$ is assumed to be Gaussian, with zero mean, variance $\boldsymbol{\Sigma}_i$, and uncorrelated between different measurements. We treat the above as a maximum a-posteriori (MAP) problem, and may additionally assume a Gaussian prior for some (or all) parameters. Under the Gaussian assumption, the MAP estimator for $\boldsymbol{x}$ is equivalent to the NLS estimator and given by

$$\boldsymbol{x}^* = \operatorname*{argmin}_{\boldsymbol{x}} \sum_i (f_i(\boldsymbol{x}) - \widetilde{\boldsymbol{y}}_i)^T \boldsymbol{\Sigma}_i^{-1} (f_i(\boldsymbol{x}) - \widetilde{\boldsymbol{y}}_i). \qquad (2.3)$$

This minimization problem can be solved by standard non-linear optimization techniques, in this case using the Levenberg-Marquardt algorithm.

Based on this abstract problem description, we now present the specific model parameters and measurement equations of the MAP-based GNSS/IMU/LiDAR-integration.

2.1 Model parameters

All sensors considered here are mounted rigidly on a moving platform. The estimable quantities $\boldsymbol{x}$ in this sensor fusion problem are then made up of three types: (1) the position $\boldsymbol{p}(t)$ and orientation $\boldsymbol{R}(t)$ of the platform itself, (2) GNSS antenna positions $\boldsymbol{l}_{a1}, \boldsymbol{l}_{a2}$, scanner boresight misalignment $\boldsymbol{M}_s$, scanner origin $\boldsymbol{l}_s$ and (3) object space parameters. To simplify presentation, the trajectory is referenced to the IMU, and the IMU coordinate frame is assumed identical to the platform frame. To capture higher frequency dynamics, trajectory spline nodes are set at the frequency of the IMU measurements. The georeferencing of the LiDAR measurements requires knowledge of the laser scanner's position and orientation relative to the reference frame of the trajectory, i.e., the IMU. Additionally, the positions of the GNSS antennas on the platform are required to relate the GNSS measurements to the trajectory. These quantities are not always (accurately) known but are constant, as all components are mounted rigidly with respect to each other. In addition to the mounting parameters, inertial sensor error calibration parameters are required to account for constant as well as time-varying errors in the accelerometer and gyroscope measurements. LiDAR correspondences may be incorporated in two ways, either implicitly by forming constraints between two measurements, or explicitly by forming constraints between a measurement and a model of the object space. Here, we take the latter approach, and explicitly model planar surfaces which are extracted from the point clouds. Each planar object is modelled by three parameters: an offset and two tilts, with

respect to its initial position and orientation. These object space model parameters are optimized jointly together with the other parameters.

Non-linear least-squares estimation involves the non-linear optimization Eq. (2.3), solving which requires initial values for the parameters. To obtain an initial trajectory, a Kalman filter is employed, which in turn requires at least an initial orientation. A suitable estimate of the roll and pitch angles may be obtained by static alignment or simply by assuming the platform is level. With dual-GNSS in an appropriate geometric configuration, it is possible to determine the initial heading angle from GNSS measurements. This requires that the GNSS antenna positions are accurately known and the RTK-GNSS solution is fixed, which is not always given at the start of data acquisition. As the low-grade IMU is unable to perform gyrocompassing, the initial heading is therefore considered unknown. A quaternion-based unscented Kalman filter (QUKF) with forward-backward smoothing is used, as it is robust against bad initial state values. The Kalman filter solution is only needed to provide initial values for the NLS adjustment, therefore its accuracy is not critical and no specific alignment procedure is required.

2.2 Measurement equations

The MLS system comprises two GNSS receivers. The respective antennas are mounted roughly along the forward axis of the vehicle, with a baseline of $\sim 3.5\,\mathrm{m}$. Using RTK correction data, a GNSS position solution is computed in real time on the device for each of the antennas. The predicted position of each antenna may be derived from the platform position $\boldsymbol{p}(t)$, the platform orientation $\boldsymbol{R}(t)$ and the GNSS antenna positions $\boldsymbol{l}_{a1}, \boldsymbol{l}_{a2}$. The GNSS position measurements of the different receivers may not arrive simultaneously, depending on how the internal receiver clock biases are applied to the output measurement timestamps. Apart from possibly different timing and the respective antenna positions, the measurement equation itself remains the same, regardless of whether one, two, or even more antennas are used. For GNSS position measurements $\widetilde{\boldsymbol{p}}_1, \widetilde{\boldsymbol{p}}_2$ at times t_1, t_2, the measurement equations are given by

$$\underbrace{\begin{matrix} \widetilde{\boldsymbol{p}}_1 \\ \widetilde{\boldsymbol{p}}_2 \end{matrix}}_{\text{measurement}} = \underbrace{\begin{matrix} \boldsymbol{p}(t_1) + \boldsymbol{R}(t_1)\,\boldsymbol{l}_{a1} \\ \boldsymbol{p}(t_2) + \boldsymbol{R}(t_2)\,\boldsymbol{l}_{a2} \end{matrix}}_{\text{model}} + \underbrace{\begin{matrix} \boldsymbol{\epsilon}_{p1} \\ \boldsymbol{\epsilon}_{p2} \end{matrix}}_{\text{noise}}, \qquad (2.4)$$

where the measurement errors $\boldsymbol{\epsilon}_p$ are assumed zero-mean and normally distributed with covariance $\boldsymbol{\Sigma}_p$. The on-board RTK processing provides an estimate of $\boldsymbol{\Sigma}_p$ along with each position measurement. The measurements of different epochs are assumed uncorrelated. This latter assumption is not always appropriate, and in such cases the error model may be adapted to account for time-correlation (Pöppl et al., 2023b).

The IMU, made up of an accelerometer and a gyroscope, provides measurements $\widetilde{\boldsymbol{f}}$ and $\widetilde{\boldsymbol{\omega}}$ of specific force $\boldsymbol{f}$ and angular velocity $\boldsymbol{\omega}$. The predicted values for specific force and angular velocity depend on platform position and orientation, and may be computed using the strap-down inertial navigation equations (cf. Groves 2013 and Pöppl et al. 2023a). The measured values are tainted by additive white noise $\boldsymbol{\epsilon}_\star$, biases $\boldsymbol{b}_\star$ and scale factors $\boldsymbol{S}_\star = \operatorname{diag}(s_{x\star}, s_{y\star}, s_{z\star})$. The measurement model for specific force and angular velocity at a time t is thus given by

$$\underbrace{\begin{matrix} \widetilde{\boldsymbol{f}} \\ \widetilde{\boldsymbol{\omega}} \end{matrix}}_{\text{measurement}} = \underbrace{\begin{matrix} (I + \boldsymbol{S}_f)\,\boldsymbol{f}(t) + \boldsymbol{b}_f(t) \\ (I + \boldsymbol{S}_\omega)\,\boldsymbol{\omega}(t) + \boldsymbol{b}_\omega(t) \end{matrix}}_{\text{model}} + \underbrace{\begin{matrix} \boldsymbol{\epsilon}_f \\ \boldsymbol{\epsilon}_\omega \end{matrix}}_{\text{noise}}. \qquad (2.5)$$

---

[1] The paper "*Trajectory estimation with GNSS, IMU, and LiDAR for terrestrial/kinematic laser scanning*" will be published in the proceedings of the Laser Radar Technology and Applications XXVIII (2023) conference.

The biases and scale factors cause errors in the trajectory which compound in time. Due to the redundant information provided by GNSS and LiDAR data, these errors may be calibrated in-run. Biases and scale factors are a sum of a time-constant component, which changes only on power cycling the device, and a time-varying component (Groves, 2013). The time-varying components are generally modelled as stochastic processes with certain characteristics. The process characteristics for the accelerometer and gyroscope bias and white noise processes are be obtained in a static calibration using Allan Variance analysis (see Farrell et al. 2022). While the scale factors may also vary in time, we model them as constant parameters for each data acquisition. This is partially motivated by the estimability of these parameters: in situations with limited platform dynamics, the time-varying biases and scale factors are hard to distinguish. This difficulty is compounded by the fact that no well-founded stochastic model for the time-varying component of the scale factor is currently available for the IMU used here.

Errors in the trajectory propagate through the georeferencing and cause discrepancies in the point clouds, which are visible in areas where point clouds acquired at different times overlap. Based on this observation, the redundant information in overlapping point clouds may be used to constrain the trajectory, as long as the observed objects remain stationary. Here, planar surfaces are used as features, which are extracted from point clouds.

The measurement model is the same as in Pöppl et al. (2023b), but the feature extraction used here is not based on voxelization. Instead, an octree representation of the point cloud is traversed from coarse to fine in order to extract both large features (e.g., facades) and small features (e.g., sidewalk curbs). At each step, an attempt is made to fit a plane using a robust plane fitting method based on Nurunnabi et al. (2015). The extracted planar features are then matched to spatially nearby other planar features in a greedy fashion. All corresponding planar features are aggregated into a planar object, which serves as a model for the physical surface. A planar feature is defined by a plane center $\widetilde{c}$ and plane normal $\widetilde{n}$, and may be considered a measurement of a planar object, which is in turn described by a plane center c and plane normal n. Under the assumption that these planar features describe the same object, they are constrained to coincide with their object plane. Specifically, three constraints are formed, regarding feature-to-object normal distance as well as feature plane normal orthogonality w.r.t. the object plane axes

$$
\begin{aligned}
\mathbf{0} &= ((\boldsymbol{c} - \widetilde{\boldsymbol{c}}) \cdot \boldsymbol{n}) &+& \epsilon_n \\
\mathbf{0} &= (\widetilde{\boldsymbol{n}} \cdot \boldsymbol{k}_1) &+& \epsilon_{k_1} \\
\mathbf{0} &= \underbrace{(\widetilde{\boldsymbol{n}} \cdot \boldsymbol{k}_2)}_{\text{constraint}} &+& \underbrace{\epsilon_{k_2}}_{\text{noise}}
\end{aligned}
\tag{2.6}
$$

The plane axes $\boldsymbol{k}_1, \boldsymbol{k}_2$ (respectively $\widetilde{\boldsymbol{k}}_1, \widetilde{\boldsymbol{k}}_2$) are chosen so that $[\boldsymbol{k}_1 \, \boldsymbol{k}_2 \, \boldsymbol{n}]$ (respectively $[\widetilde{\boldsymbol{k}}_1 \, \widetilde{\boldsymbol{k}}_2 \, \widetilde{\boldsymbol{n}}]$) are orthonormal, but are otherwise arbitrary. A feature plane is internally stored as center $\widetilde{\boldsymbol{c}}_s$ and normal $\widetilde{\boldsymbol{n}}_s$ in the scanner coordinates. To form the constraints Eq. (2.6) in object space, it is transformed into physical coordinates using the georeferencing equation

$$
\begin{aligned}
\widetilde{\boldsymbol{c}} &= \boldsymbol{R}(t)\, \boldsymbol{M}_s\, (\widetilde{\boldsymbol{c}}_s + \boldsymbol{l}_s) + \boldsymbol{p}(t), \\
\widetilde{\boldsymbol{n}} &= \boldsymbol{R}(t)\, \boldsymbol{M}_s\, \widetilde{\boldsymbol{n}}_s.
\end{aligned}
\tag{2.7}
$$

The random errors occurring in Eq. (2.6) are assumed to be uncorrelated and Gaussian. Their covariances are derived from the PCA results, but scaled in order to account for angle of incidence and laser footprint.
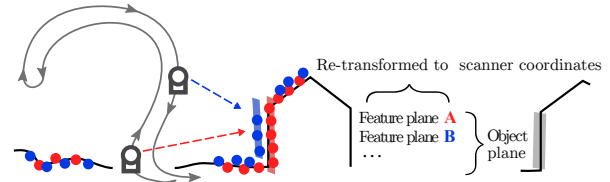

Figure 1. Areas which are not occluded are scanned multiple times during multiple passes. *Feature planes* are extracted separately from points acquired during different passes, and the corresponding feature planes are then matched to a single *object plane*.
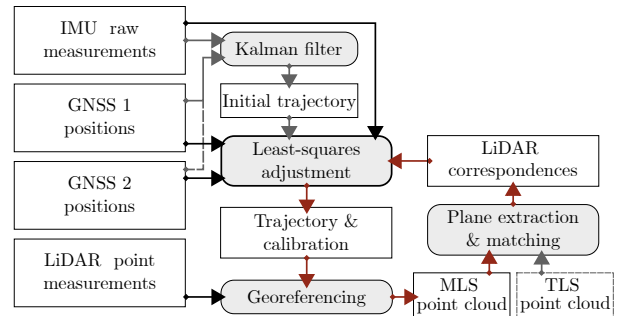

Figure 2. Full processing workflow for the GNSS/IMU/LiDAR integration. The steps marked in red may optionally be iterated. If reference data is available, in this case from a TLS acquisition campaign, it may be incorporated in the adjustment.

Point cloud data from other sources may be introduced into the adjustment as control information. In this case, planes are extracted from the control point cloud as described above, but the planar object parameters are not optimized and stay fixed to their initial value.

2.3 Processing workflow

The NLS adjustment is the core of the processing workflow, with the full pipeline depicted in Fig. 2. First, the Kalman smoother is used to obtain an initial trajectory, which is refined in a first NLS adjustment. Then, an approximate point cloud is computed, from which planar surfaces are extracted. Planar surfaces observed at different times are matched and these correspondences are used together with the raw IMU data and GNSS positions in the NLS adjustment. Optionally, the plane extraction may be re-run and the adjustment restarted. This is useful in a calibration scenario, where the laser scanner calibration parameters are unknown and the initial point cloud is highly inaccurate.

In the data acquisitions discussed below, the mounting position of the second antenna changes depending on the exact system set-up. The following approach ensures the system is adequately calibrated for its final purpose:

1. Calibration of boresight angles and antenna positions using a special calibration dataset.

2. Re-calibration of 2nd antenna position in the field if system set-up changes.

3. During normal data acquisition, mounting parameters stay fixed.

3. CASE STUDIES

The viability of the proposed method was demonstrated on two different datasets acquired with a prototype MLS system setup.
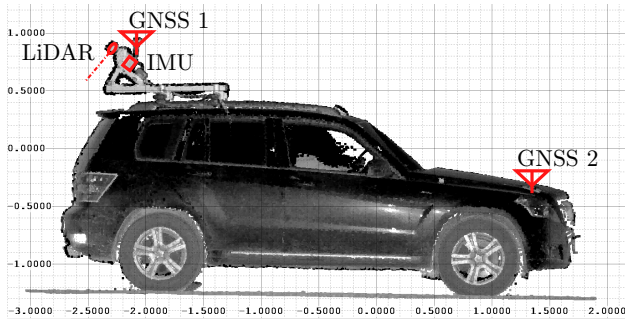
Figure 3. MLS system setup on car roof with LiDAR, IMU and 2 GNSS antennas. The distance between the GNSS antennas is $\sim 3.5\,\text{m}$.

A special calibration dataset (Fig. 4) is used to obtain initial parameters for the antenna positions and the LiDAR boresight angles. For this study area, reference data from terrestrial laser scanning is available and used during boresight calibration and as comparison for the kinematically acquired point cloud. The second data set (Fig. 10) is a use case example of mobile laser scanning in a mining environment. This is a 40 minute long dataset where the impact of (1) single antenna vs. dual antenna GNSS and (2) the use of LiDAR-derived observations on (a) the consistency of the point cloud and (b) the estimated platform trajectory is analyzed.

The MLS system used here is based on a *RIEGL* miniVUX laser scanner, together with a ultra low-cost IMU and two low-cost GNSS receivers. The LiDAR, IMU and one GNSS antenna are fixed to the roof mount of a car or truck. The second antenna is mounted either on the car's engine hood using a magnetic backplate (Fig. 3) or also on the car roof (Fig. 9). For the data acquisitions discussed here, the GNSS receivers were operated purely in RTK mode due to limitations related to the technical implementation.

3.1 Calibration and preliminary evaluation

The first dataset (Fig. 4) was acquired in Horn, Lower Austria, in a suburban area. This dataset will be used for calibrating the IMU-LiDAR boresight angles. An accurate boresight calibration is a requirement for accurate georeferencing. Boresight calibration based on adjustment of the LiDAR data itself requires a large enough overlap in the scan data and suitable object space geometry. For an approach based on corresponding planar surfaces, the environment must of course contain sufficient planar surfaces of different orientations. This dataset has high overlap, features many planar surfaces (buildings), and the GNSS/RTK base station is close by (less than 1 km). However, the scanning geometry of the laser scanner together with the geometry of such a suburban environment makes it difficult to estimate the pitch component of the IMU-LiDAR boresight angles. This is made worse by the fact that the IMU used here has high noise as well as high drift. To improve the boresighting, we use a reference point cloud from terrestrial laser scanning (TLS) for the calibration procedure.

The TLS data (Fig. 5) consists of 1.8 billion points acquired from 100 static scan positions. All data was co-registered together, without use of additional control points. The feature extraction method described above is used to extract planar features from this reference point cloud. An example is shown in Fig. 6. The trajectory and system calibration (IMU-LiDAR misalignment and antenna positions) are estimated together as described above. The process of georeferencing, feature extraction, feature matching and NLS adjustment is repeated until the

boresight angles and antenna positions are stable (i.e., until they change less than 5 mdeg and 0.5 mm, respectively).

Figure 4. Top-down reflectance view of the MLS calibration dataset. The trajectory is shown in red. TLS data is available for the area on the lower left.
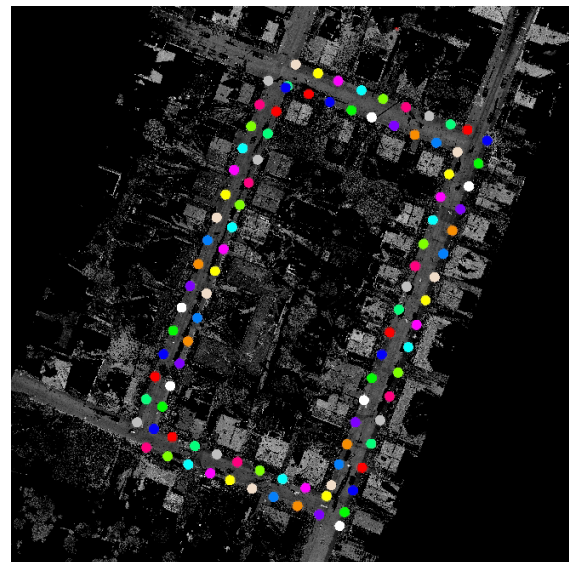

Figure 5. Top-down reflectance view of the TLS dataset with 100 static scan positions shown as colored dots.

The resulting trajectory and point cloud are shown in Fig. 4. A voxelization with voxel size 0.25 m is computed for each point cloud, and a best-fit plane is estimated for all points within each voxel. To evaluate the fit of the MLS point cloud with respect to the TLS point cloud, the normal distances between the MLS voxel centers and the TLS voxels best-fit plane are computed and shown in Fig. 7. The discrepancies are below 1 cm, apart for spurious points on e.g., vegetation. Note that this is not a measure of absolute accuracy, as the TLS data used for comparison was also used for the adjustment itself. The residual differences, which exist even after adjustment, show there is still some inconsistency between the MLS and TLS data. This might be partially due to inaccuracies in the TLS data. From repeat TLS acquisitions in this area, we generally expect the TLS data to be accurate to within 1 cm. Fig. 8 shows the standard deviation of each voxels' points' normal distances w.r.t. to own best-fit plane. These standard deviation are below 1.5 cm, with a larger standard deviation in the same areas where a larger discrepancy is visible in Fig. 7.

In order to obtain a more quantitative measure, the normal distances of all MLS points to (a) the TLS best-fit planes and (b)
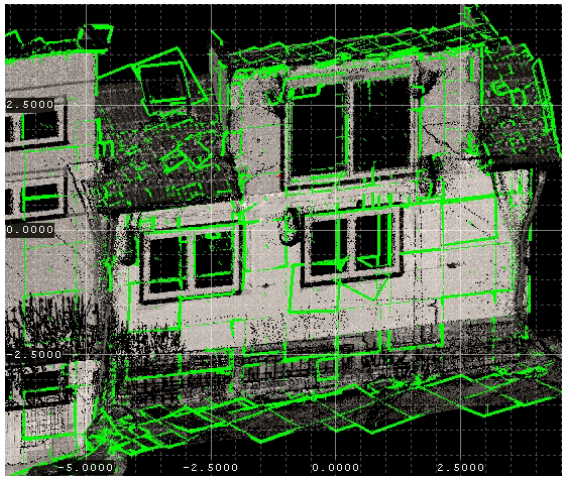
Figure 6. Example of planes (green) extracted from the TLS point cloud (reflectance, grayscale).
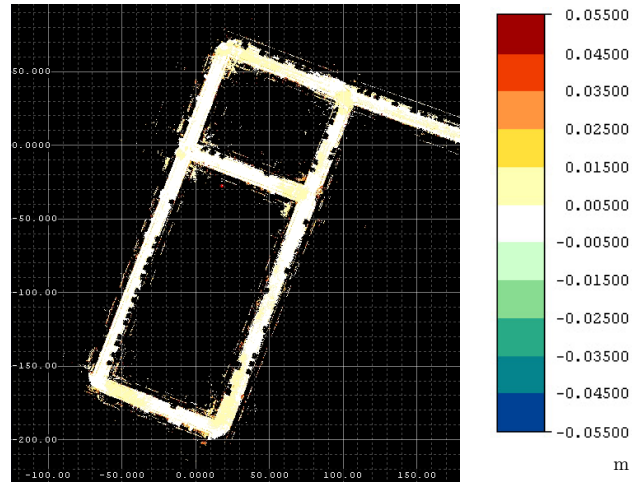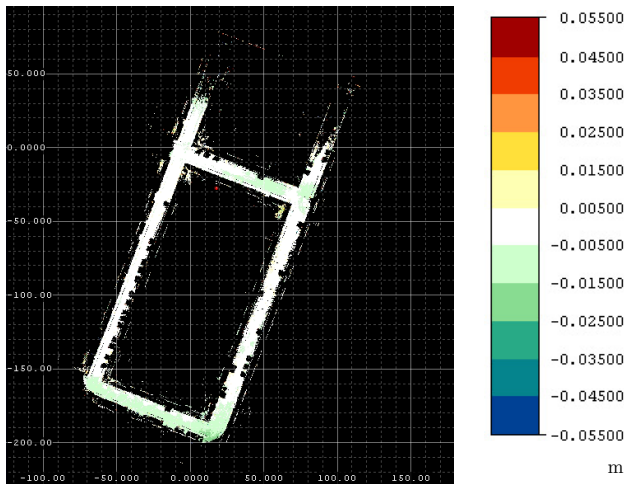

Figure 7. Normal distance of MLS voxel centers to the corresponding TLS voxel best-fit plane, per voxel

the MLS best-fit planes are computed. Table 1 shows the minimum MIN, root mean square error RMSE and maximum MAX distances. The minimum and maximum are limited by 0.25 m, as this is the voxel size and maximum search radius used for the comparison. As these statistics are tainted by points on e.g., moving objects or vegetation, robust statistics of the 5-95 percentiles are also given. The robust values, specifically the $RMSE_5^{95}$ of 4 mm agree with Fig. 8. In a manual evaluation of planar surfaces (e.g., facades and roads) in the dataset, the precision is better than $\sigma = 5$ mm.

3.2 Application in a mining environment

The second dataset was acquired in Sishen mine, a large open-pit iron ore mine located in central South Africa. The same *RIEGL* miniVUX laser scanning system was used, this time mounted on the roof rack of a jeep (Fig. 9). The data acquisition consists of a ~ 20 km stretch of road, depicted in Fig. 10. The point cloud and trajectory are shown in Fig. 11 and examples of the acquired point clouds are given in Fig. 12. The IMU-LiDAR boresight misalignment is known from the previous calibration. However, due to the system being set up on a different vehicle, the position of the second GNSS antenna is different to the previous setup, and is estimated on a separate dataset. Both GNSS antenna positions and the IMU-LiDAR boresight are held constant for

Figure 8. Standard deviations of the normal distances of MLS points to their voxels best-fit plane, per voxel.

	MLS to MLS	MLS to TLS
MIN_0	-0.2485	-0.2495
$RMSE_0^{100}$	0.0170	0.0335
MAX^{100}	0.2477	0.2492
MIN_5	-0.0103	-0.0408
$RMSE_5^{95}$	0.0041	0.0106
MAX^{95}	0.0100	0.0448

Table 1. Distances of MLS points w.r.t. the MLS or TLS data best-fit planar surfaces using a 0.25 m voxelization. The minimum, root mean square error, and maximum of the distances are given for all data, as well as for a robust subset with the bottom/top 5% cut off.

the processing of the dataset discussed below.

As no reference data is available, the following evaluation is based on analyzing the consistency of the point cloud as well as properties of the trajectory for different processing scenarios. Namely, we will compare the GNSS/IMU-integration with the GNSS/IMU/LiDAR-integration for both single antenna and dual antenna configurations, resulting in four scenarios:

- G_1I: GNSS/IMU integration, one antenna,
- G_1IL: GNSS/IMU/LiDAR integration, one antenna,
- G_2I: GNSS/IMU integration, two antennas,
- G_2IL: GNSS/IMU/LiDAR integration, two antennas.

In the first two cases, only data from the main GNSS antenna (located above the scanner) is used. The focus of this analysis

Figure 9. MLS system set-up mounted on a jeep. The laser scanner is mounted in the back, together with the primary GNSS antenna. The secondary GNSS antenna is mounted in front, above the driver, with a distance of ~ 3.8 m between the antennas.
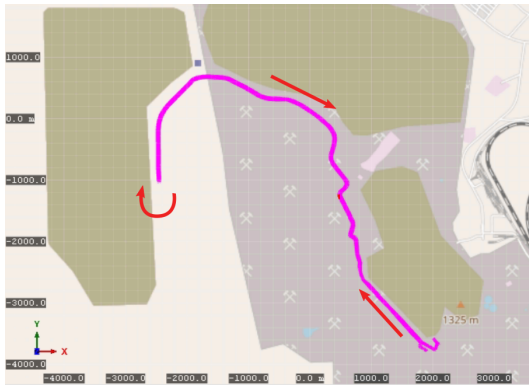
Figure 10. The trajectory consists of forward and backward passes along the same road, and starts/ends in the southeast.

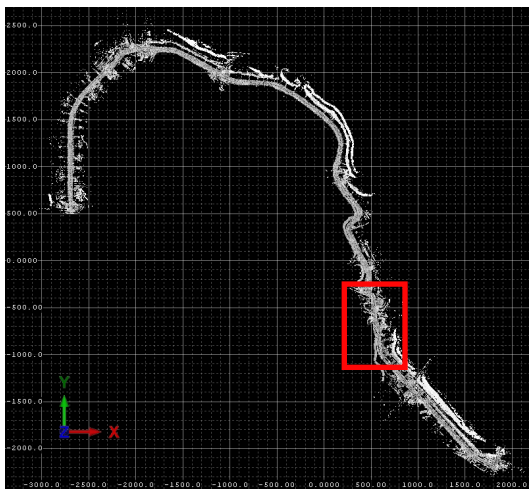Figure 12. Examples of the point cloud (grayscale, reflectance).

Figure 11. Point cloud (grayscale, reflectance) shows mainly road and berms due to limited visibility. The area marked in red shown below for comparison of the height differences.
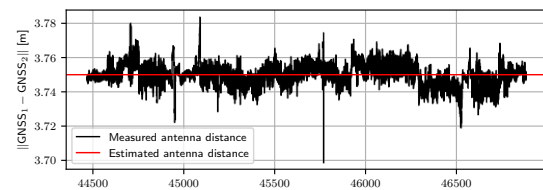

Figure 13. Distance between the two GNSS antennas, as measured by the RTK-GNSS.

is on two aspects: the impact of (a) the second GNSS antenna, and (b) the LiDAR measurements on the point cloud and the trajectory.

The integration architecture discussed here makes use of loosely coupled GNSS, with the GNSS operating in RTK mode. This means for optimal performance, both good satellite reception as well as good reception of the RTK correction signal is required. Both of these requirements are at least partially given, and the RTK processing reports a fix for the full duration, apart from a short initialization phase in the beginning. As a quality check of the GNSS measurements, we may look at the measured distance between the two GNSS antennas (Fig. 13). For most of the data acquisition, this differs less than ± 1 cm from the distance between the previously estimated antenna positions. To make the integration more robust, GNSS measurements where the difference exceeds ± 2.5 cm are not used for in the trajectory estimation.

As an evaluation of the consistency of the point cloud, Fig. 14 shows the height differences between the forward and the backward passes. After adjustment of all data (GNSS, IMU and LiDAR), the consistency is good with a maximum discrepancy of 2.5 cm. Only some segments the road area is scanned both in the forward and in the backward pass, as berms in the middle of the road limit visibility of the road surface (Fig. 15). There is little improvement in the height difference when comparing

the single-antenna and the dual-antenna GNSS/IMU integration, and of the single-antenna and dual-antenna GNSS/IMU/LiDAR integration, respectively. However, the addition of the LiDAR measurements in the adjustment significantly reduces the height differences for both scenarios. The height differences alone will not show all trajectory errors. Especially errors in the heading angle, which we seek to minimize with the addition of the second antenna, are not very visible in the height component. The dataset contains a small number of buildings and other man-made structures, the facades of which are suitable at least for a qualitative evaluation. Fig. 16 shows a vertical view of such a building facade, with points from all four processing scenarios. For an ideal plane and error-free measurements, all points would lie on a horizontal line. The spread of the points from the $G_1 IL$ (red), $G_2 I$ (green), $G_2 IL$ (blue) are comparable, but the $G_1 I$ (yellow) points have a much higher spread. This suggests errors in the latter trajectory, which are corrected either by inclusion of the second GNSS antenna or by inclusion of the LiDAR constraints.

Further insight may be gained by analyzing the differences between the trajectories from these four scenarios (Fig. 17). Overall, the difference between the GI trajectory and the GIL trajectory is larger for the single-antenna scenario than for the dual-antenna scenario. Note that the inclusion of LiDAR measurements in the dual-GNSS scenario leads to a correction of the roll angle, but the pitch and yaw remain relatively stable. This is due to the geometry of the GNSS antennas: with two antennas mounted along the forward axis of the vehicle, the pitch and yaw are estimable from the antenna positions while the roll is not. The GIL trajectories of both scenarios agree very well whenever laser data is available, implying that the GIL trajectories are more correct. Conversely, the addition of the second antenna seems to provide benefit mostly in the first stage, i.e., GNSS/IMU integration. However, as the LiDAR correspondences are established based on georeferencing with the GNSS/IMU trajectory, a better initial trajectory results in bet-

(a) G_1I (b) G_2I

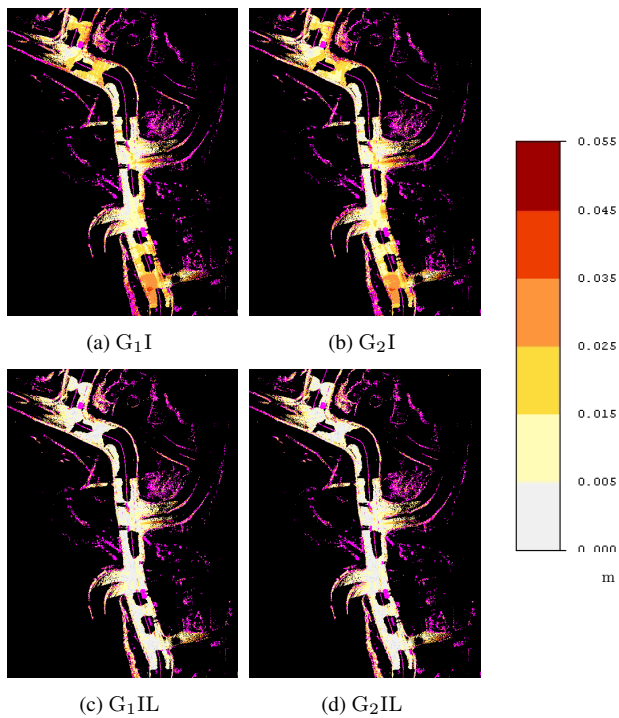(c) G_1IL (d) G_2IL

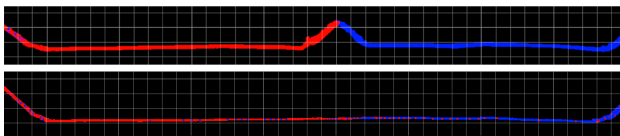Figure 14. Height differences of the four scenarios.

Figure 15. Berms in the middle of the road limit the overlap between point clouds from forward (red) and backward (blue) pass. In some areas, the full street is visible from both sides of the street.

ter correspondences. This is not as critical here, because most of the suitable object space geometry is located near the road, and due to the lower range, errors in orientation have a limited impact.

4. DISCUSSION

In conclusion, the results suggest that by tightly coupling LiDAR and IMU, even low-grade inertial sensors may be used for mobile laser scanning. A precision of $\sigma \leq 5$ mm is achieved, as measured by the spread of points on planar surfaces in the test area. Furthermore, the use of the second GNSS antenna limits drift in a GNSS/IMU integration as expected, but this has less impact on the final point cloud in a LiDAR-integrated adjustment. While the second GNSS antenna helps stabilize the initial GNSS/IMU trajectory and therefore aids the plane extraction, it does not significantly improve the result after GNSS/IMU/LiDAR integration, provided good LiDAR correspondences are available. This is likely due to the strong constraints on the heading imposed by the LiDAR correspondences.

In future work, the GNSS processing will be done in post-processing with precise ephemerides to avoid the problem of missing RTK correction data and to improve positioning quality. Also, further evaluations need to be done in order to quantify the absolute accuracy of the methodology.
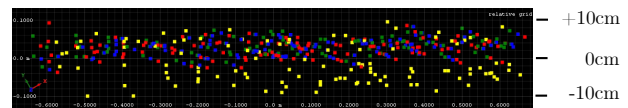

Figure 16. Vertical view of a facade with points from all four point clouds: G_1IL (red), G_2I (green), G_2IL (blue) and G_1I (yellow). All points lie within ± 10 cm, but the spread of the G_1I points is higher compared to the other scenarios.

References

Brun, A., Cucci, D. A., Skaloud, J., 2022. LiDAR Point–to–Point Correspondences for Rigorous Registration of Kinematic Scanning in Dynamic Networks. *ISPRS Journal of Photogrammetry and Remote Sensing*, 189, 185–200.

Chang, L., Niu, X., Liu, T., Tang, J., Qian, C., 2019. GNSS/INS/LiDAR-SLAM Integrated Navigation System Based on Graph Optimization. *Remote Sensing*, 11(9), 1009.

Cucci, D. A., Rehak, M., Skaloud, J., 2017. Bundle Adjustment with Raw Inertial Observations in UAV Applications. *ISPRS Journal of Photogrammetry and Remote Sensing*, 130, 1–12.

Farrell, J. A., Silva, F. O., Rahman, F., Wendel, J., 2022. Inertial Measurement Unit Error Modeling Tutorial: Inertial Navigation System State Estimation with Real-Time Sensor Calibration. *IEEE Control Systems*, 42(6), 40–66.

Glira, P., Pfeifer, N., Briese, C., Ressl, C., 2015. A Correspondence Framework for ALS Strip Adjustments Based on Variants of the ICP Algorithm. *Photogrammetrie - Fernerkundung - Geoinformation*, 2015(4), 275–289.

Groves, P. D., 2013. *Principles of GNSS, Inertial, and Multisensor Integrated Navigation Systems*. GNSS Technology and Application Series, 2nd ed. edn, Artech House, Boston.

Kim, M.-J., Kim, M.-S., Shin, S. Y., 1995. A General Construction Scheme for Unit Quaternion Curves with Simple High Order Derivatives. *Proceedings of the 22nd annual conference on Computer graphics and interactive techniques - SIGGRAPH '95*, ACM Press, Not Known, 369–376.

Nurunnabi, A., West, G., Belton, D., 2015. Outlier Detection and Robust Normal-Curvature Estimation in Mobile Laser Scanning 3D Point Cloud Data. *Pattern Recognition*, 48(4), 1404–1419.

Pöppl, F., Neuner, H., Mandlburger, G., Pfeifer, N., 2023a. Integrated Trajectory Estimation for 3D Kinematic Mapping with GNSS, INS and Imaging Sensors: A Framework and Review. *ISPRS Journal of Photogrammetry and Remote Sensing*, 196, 287–305.

Pöppl, F., Pfennigbauer, M., Ullrich, A., Mandlburger, G., Neuner, H., Pfeifer, N., 2023b. Modelling of GNSS Positioning Errors in a GNSS/INS/LiDAR-integrated Georeferencing. *Publikationen Der Deutschen Gesellschaft Für Photogrammetrie, Fernerkundung Und Geoinformation e.V.*, 183–196.

Wang, Chen, Zhu, Liu, Li, Zheng, 2019. A Survey of Mobile Laser Scanning Applications and Key Techniques over Urban Areas. *Remote Sensing*, 11(13), 1540.
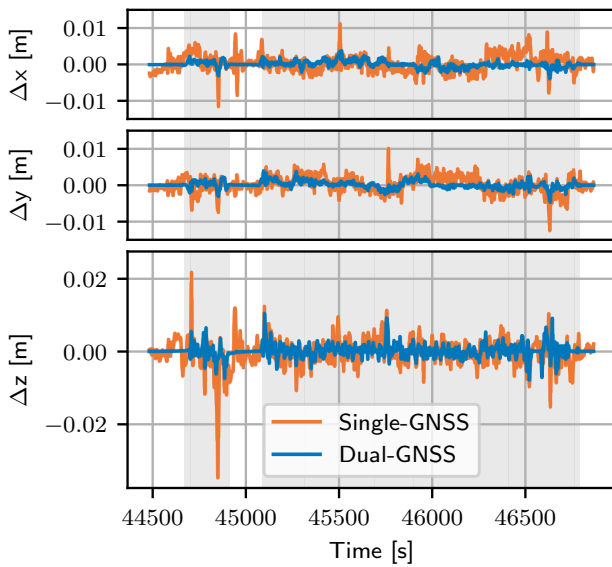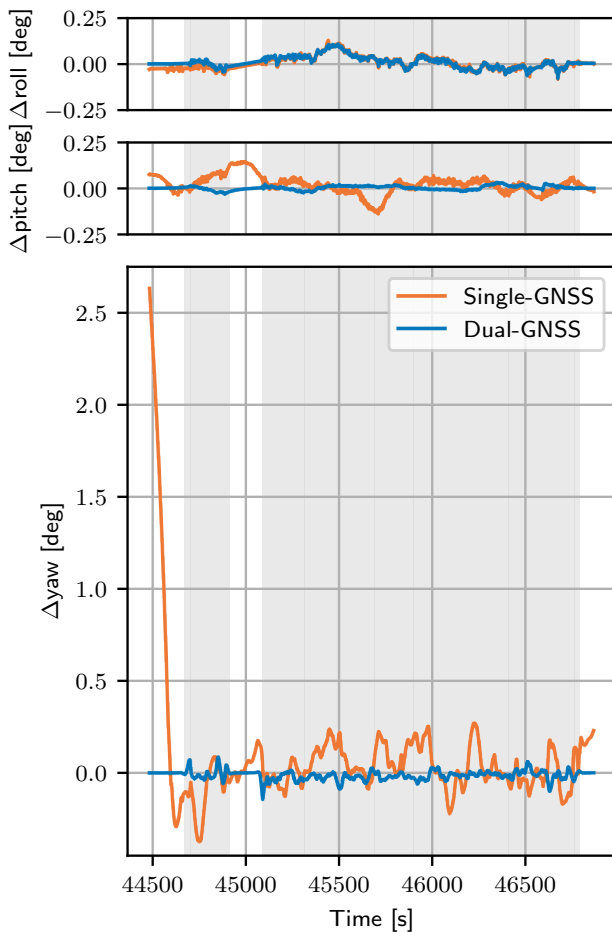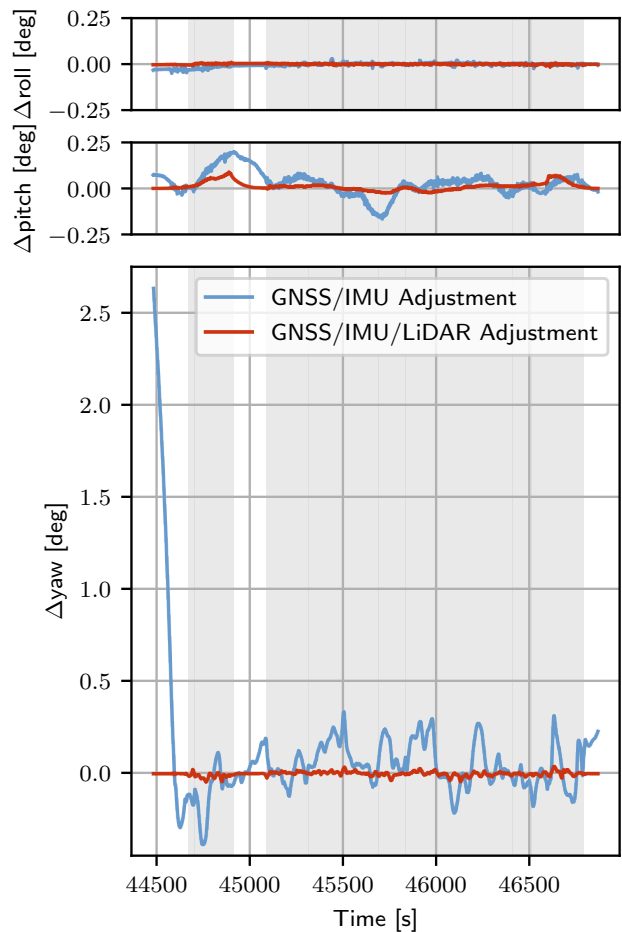
(a) Position difference between GNSS/IMU and GNSS/IMU/LiDAR integration, respectively for single-antenna and dual-antenna scenarios.
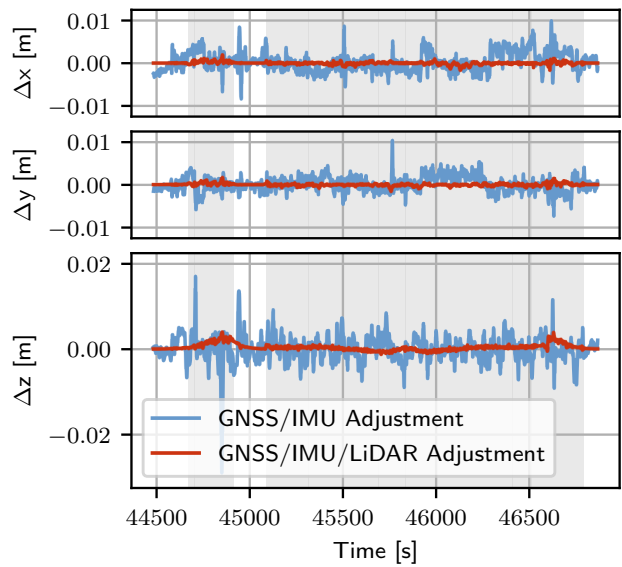
(b) Position difference between single-antenna and dual-antenna scenarios, respectively for GNSS/IMU and GNSS/IMU/LiDAR integration.

(c) Orientation difference between GNSS/IMU and GNSS/IMU/LiDAR integration, respectively for single-antenna and dual-antenna scenarios.

(d) Orientation difference between single-antenna and dual-antenna scenarios, respectively for GNSS/IMU and GNSS/IMU/LiDAR integration.

Figure 17. Differences in position (above) and orientation (below) between the GNSS/IMU and GNSS/IMU/LiDAR integration (left) and between single-antenna and dual-antenna scenarios (right). Time intervals where LiDAR data is available are shaded gray.